Rocky Worlds DDT: HST Data Analysis Report for GJ 3929, part II

Leonardo Dos Santos, John H. Debes | *HST Data Analysis Team*
Néstor Espinoza, Hannah Diamond-Lowe | *RWDDT CIT Leads*

HST observed Visits 1-3, 5, 6, and 56-60 of the program for GJ 3929 (PID 17904) between January 30 and March 4, 2026. Visit 1-3 were designed with four consecutive orbits with COS/G130M to obtain a time-series to detect FUV flares in GJ 3929 and provide spectral coverage. Visit 5 provided spectral coverage with COS/G160M, while Visit 6 aimed to cover the NUV and optical spectrum of GJ 3929 with STIS. There was a partial failure of Visit 6, for which we obtained repeat exposures in Visit 56. Visits 57-60 were single-orbit repeats of the failed exposures of Visits 7 and 8, which were designed to obtain the first Lyman-α spectra of GJ 3929.

These observations are fundamental to constraining the high-energy output of this host M dwarf in the UV, which can be applied to planetary models of atmospheric escape, as well as photochemistry if a planetary atmosphere is present. Along with each data analysis report, we also produce high-level science products (HLSPs) that are hosted on MAST, which will include the co-added 1-D spectrum of GJ 3929, a model for the intrinsic stellar Lyman-α emission, and the time-series fluxes of all observations obtained in photon-counting (TIME-TAG) mode.

More details about the observing modes, technical justifications and decisions are available in the RWDDT Scheduling Report for GJ 3929 (Debes et al., 2025). The observing log of the visits discussed in this report is shown in Table 1.

Table 1: Observations log of Visits 1-3, 5, 6 and 56-60 of PID 17904.

Visit	Dataset	Mode	Start Date & Time	Exposure time (s)	Status
1	LFKB01010	COS/G130M	2026-01-30 21:10:37	9146.528	Pass
2	LFKB02010	COS/G130M	2026-02-10 09:40:26	9146.368	Pass
3	LFKB03010	COS/G130M	2026-02-14 10:47:58	9146.400	Pass
5	LFKB05010	COS/G160M	2026-02-15 07:18:45	8999.264	Pass
6	OFKB06010	STIS/G230L	2026-02-02 22:51:28	2065.200	Pass
	OFKB06020	STIS/G230L	2026-02-03 00:13:09	0.0	Fail
	OFKB06030	STIS/G430L	2026-02-03 00:46:42	1.505	Fail
	OFKB06040	STIS/G750L	2026-02-03 00:52:35	1.537	Fail
	OFKB06050	STIS/G750L Flat	2026-02-03 00:58:13	50.0	Pass
56	OFKB56010	STIS/G230L	2026-03-04 06:46:54	1183.198	Pass
	OFKB56020	STIS/G430L	2026-03-04 07:14:36	60.0	Pass
	OFKB56030	STIS/G750L	2026-03-04 07:20:29	20.0	Pass
	OFKB56040	STIS/G750L Flat	2026-03-04 07:25:04	50.0	Pass
57	OFKB57010	STIS/G140M	2026-02-22 03:47:30	2040.176	Pass
58	OFKB58010	STIS/G140M	2026-02-26 01:51:44	2040.191	Pass
59	OFKB59010	STIS/G140M	2026-03-03 05:42:27	0.0	Fail
60	OFKB60010	STIS/G140M	2026-03-03 07:16:30	2040.170	Pass

1 Data quality

We received AlertObs notifications for Visits 6 and 59. In the former, the Fine Guidance Sensors (FGS) did not reacquire the guide stars at the second orbit on February 3, 2026 00:06. Thus, the shutter did not open and no exposure was performed (hence the zero exposure time in Table 1). The subsequent science exposures failed as well. A repeat of the failed orbits of Visit 6 were successfully obtained in Visit 56. As for Visit 59, the FGS could not acquire the guide stars on March 3, 2026 05:28, so the shutter did not open and no flux was measured. We did not request a repeat of this visit because we deemed that the signal-to-noise ratio (SNR) in the blue and red wings of the Lyman-α line were high enough to perform a reliable reconstruction of the intrinsic stellar Lyman-α emission (see Sections 2.2 and 3.1).

We do not observe any significant effects of jitter pointing trends in the successful observations. We present the time series of jitter vectors in Figures 15 to 23. The dataset `OFKB56030` is affected by a potential cosmic ray in the stellar trace around 10 000 Å. For future observations, we recommend using the option `CR-SPLIT` when preparing the Phase II files of STIS/CCD exposures.

2 Data Reduction

2.1 Spectral analysis

M dwarfs are generally faint targets in the far-UV (FUV) because they lack a detectable continuum. Since STIS first order spectra are not necessarily placed on the same trace position across different observations, the instrument's pipeline utilizes a cross-correlation technique to find the stellar trace and extract the spectrum at the correct cross-dispersion position. The low UV fluxes of M dwarfs frequently cause the STIS pipeline to identify the stellar trace at incorrect positions, thus we need to manually extract the spectrum. We followed the data reduction steps explained in Dos Santos et al. (2025) to extract STIS/G140M spectra. There was no need to perform custom extraction in the COS/FUV data and the STIS/NUV-MAMA or STIS/CCD data.

The STIS/CCD data obtained with the G750L grating exhibit fringing patterns that require manual correction (Figure 1). We followed the de-fringing tutorial[1] of the `stistools` package to perform this correction. Furthermore, we identified one artifact in the extracted G750L spectrum near 10 000 Å that is likely caused by a cosmic ray hit (Figure 2). To correct for this artifact, we first identify this affected pixels utilizing an IQR (Interquartile Range) filtering algorithm within a range of 40 pixels around the artifact. Then, we interpolate the values of the affected pixels to the surrounding unaffected pixels.

2.2 Lyman-α reconstruction

Since the intrinsic Lyman-α stellar emission is partially absorbed by the ISM, we need to reconstruct it in order to accurately estimate the stellar UV output. We perform this reconstruction using the same algorithm as used in Dos Santos et al. (2025) and Youngblood et al. (2016). Shortly, It consists of simultaneously fitting the the stellar intrinsic emission and the ISM absorption using the `emcee` sampler (Foreman-Mackey

[1] Available in `https://stistools.readthedocs.io/en/latest/defringe_guide.html`.

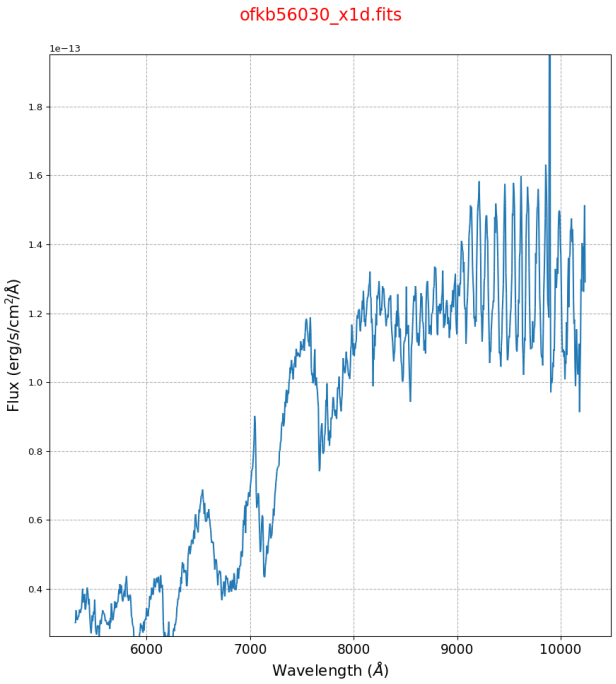

Figure 1: Fringing pattern is observed in wavelengths longer than $\sim$ 8 000 Å of STIS/G750L exposures.

et al., 2013). We model both the stellar Lyman-α line and the ISM absorption with Voigt functions and we assume that the stellar emission does not have self-absorption, since M dwarfs are not expected to produce such features (Youngblood et al., 2016). We also fix the stellar radial velocity to the value measured in the literature (10.14 km s^{-1}, Fouqué et al., 2018) and assume that there is only one ISM cloud in the line of sight.

2.3 Time-series analysis

All UV observations of GJ 3929 in the RWDDT program were executed in photon-counting mode, or `TIME-TAG`. The Rocky Worlds Utils codebase[2] possesses a dedicated time-series analysis tool that enables the user to create light curves of flux integrated over user-defined wavelength ranges at any temporal resolution within the precision of the STIS and COS instruments. For the RWDDT program, we produced light curves with a temporal resolution of 5 s for all `TIME-TAG` observations. For Lyman-α observations, we produced light curves for the blue and red wings. For every other observations, we integrate fluxes in the entire wavelength available and mask out ranges with geocoronal contamination. We do not perform corrections for telescope breathing or other systematic effects.

[2]Available in `https://github.com/spacetelescope/rocky-worlds-utils`.

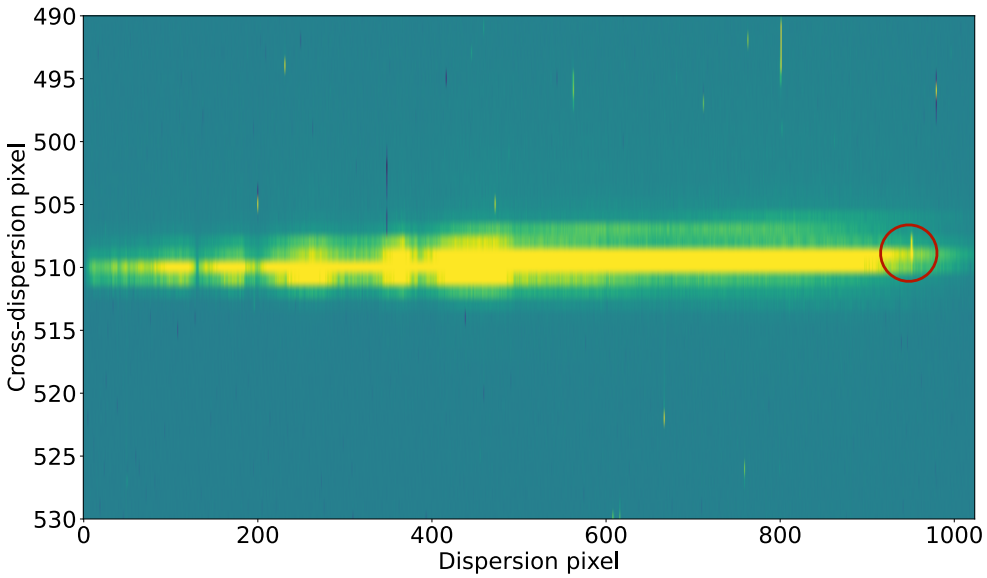

Figure 2: A cosmic ray hit on the stellar spectral trace is observed near dispersion pixel 950.

3 Combined science products

3.1 Spectrum of GJ 3929

We utilized the HSLA codebase (Sankrit et al., 2025) to co-add and abut all the final-stage HST observations obtained in this program to produce a high-fidelity spectral energy distribution (SED) of GJ 3929, which we present in Figure 3.

The posterior distribution of the parameters that define the Lyman-α emission, the Lorentzian amplitude (a_L), the FWHM of the Lorentzian component (FWHM_L), the FWHM of the Gaussian component (FWHM_G), the neutral H column density (n_{HI}), the ISM temperature (T_{ISM}) and the line-of-sight velocity of the ISM ($v_{\mathrm{ISM,LOS}}$), are presented in Table 2. The retrieved intrinsic Lyman-α line of GJ 3929 is shown in Figure 4.

Table 2: Intrinsic stellar Lyman-α and ISM parameters inferred from the data.

Parameter	95% posterior bounds
$\log a_L$ (erg s^{-1} cm^{-2} Å^{-1})	$-14.624^{+0.228}_{-0.303}$
FWHM_L (km s^{-1})	$23.373^{+13.902}_{-10.698}$
FWHM_G (km s^{-1})	$188.356^{+30.591}_{-29.674}$
$\log(n_{\mathrm{HI}})$ (cm^{-3})	$18.186^{+0.200}_{-0.205}$
T_{ISM} (K)	$9631.170^{+4766.285}_{-6813.061}$
$v_{\mathrm{ISM,LOS}}$ (km s^{-1})	$-29.163^{+2.732}_{-0.773}$

3.2 Light curves

We present the resulting light curves of the HST observations of GJ 3929 in Figures 5 to 14. Segments A and B correspond to the two physical detectors of COS, which have a gap between them. We detected a potential flare in Visit 3, near the middle of

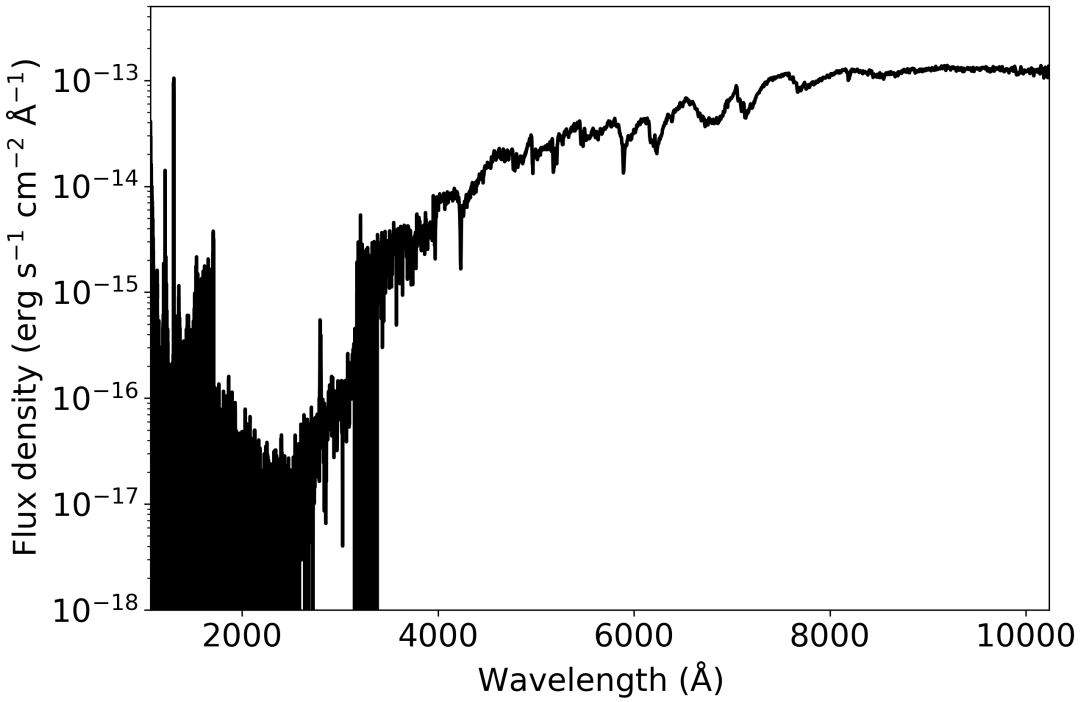

Figure 3: Full spectral energy distribution of GJ 3929 as observed in the program.

the last orbit in the time series – see the zoom-in the flare in Figure 8. The host star seems to be otherwise quiet.

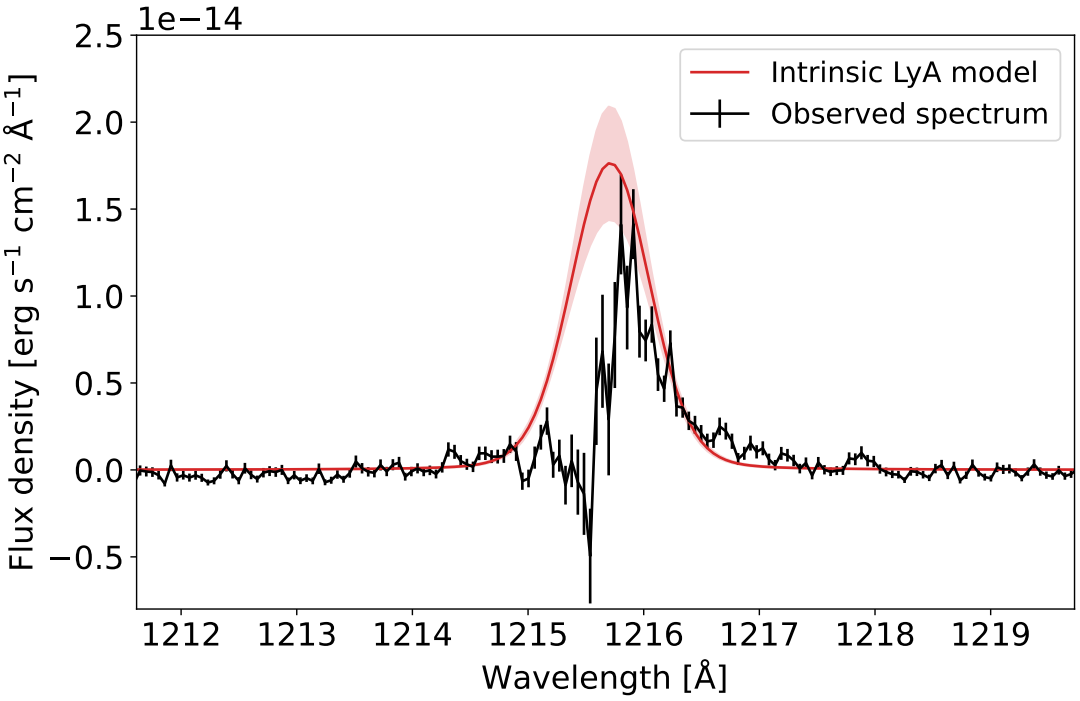

Figure 4: Co-added Lyman-α spectrum of GJ 3929 from all successful visits (black) and inferred intrinsic emission without ISM absorption (red).

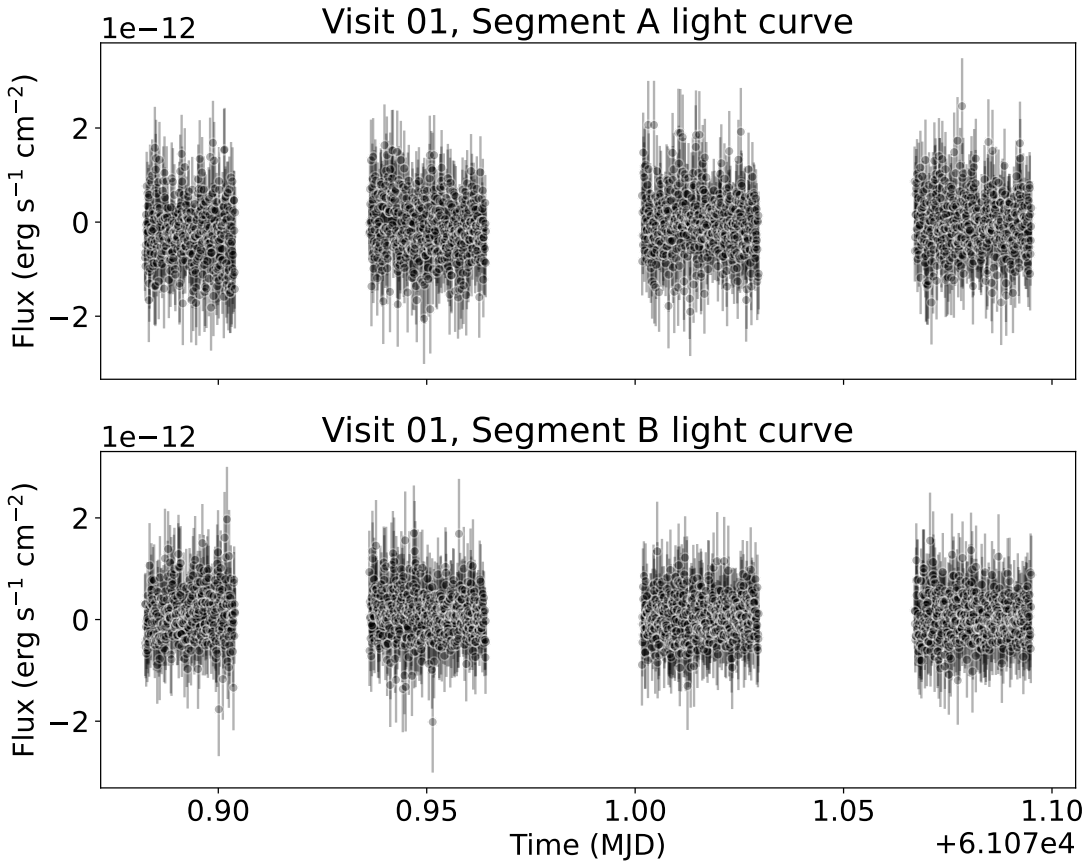

Figure 5: Light curves of Visit 1. Segment A corresponds to wavelengths [1230, 1365] Å and Segment B to [1140, 1214] Å.

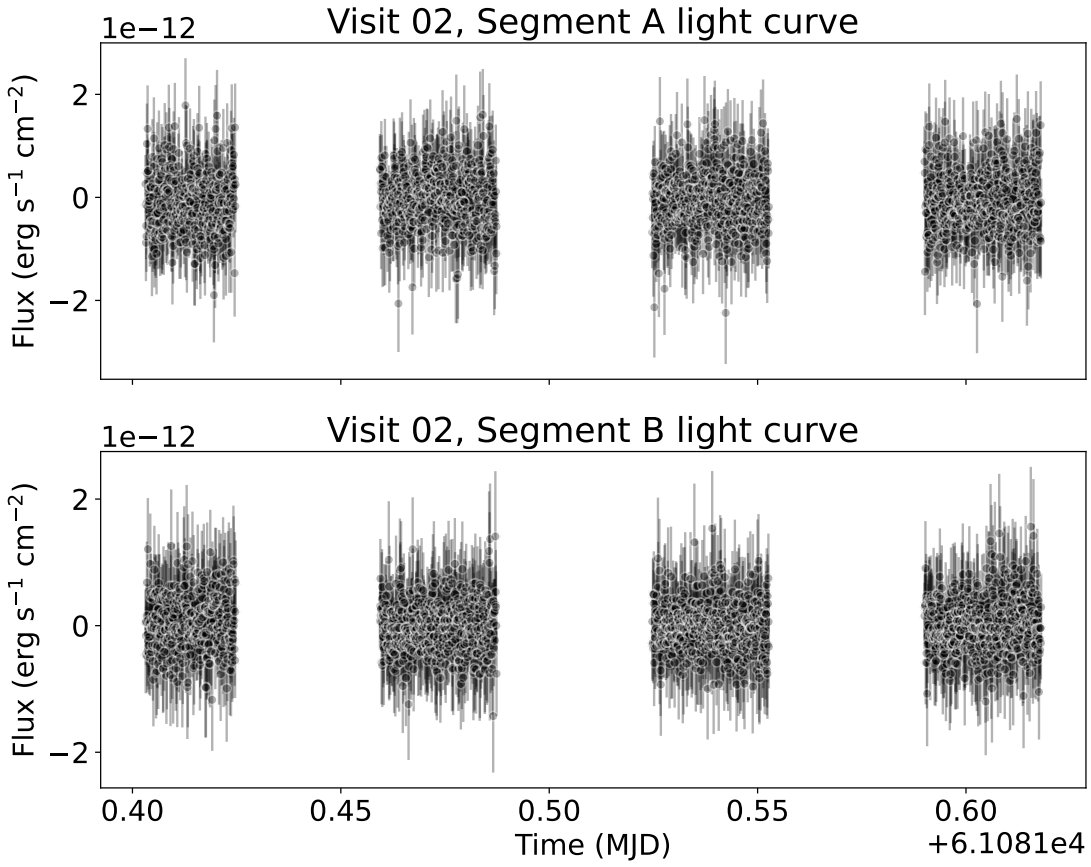

Figure 6: Light curves of Visit 2. Segment A corresponds to wavelengths [1230, 1365] Å and Segment B to [1140, 1214] Å.

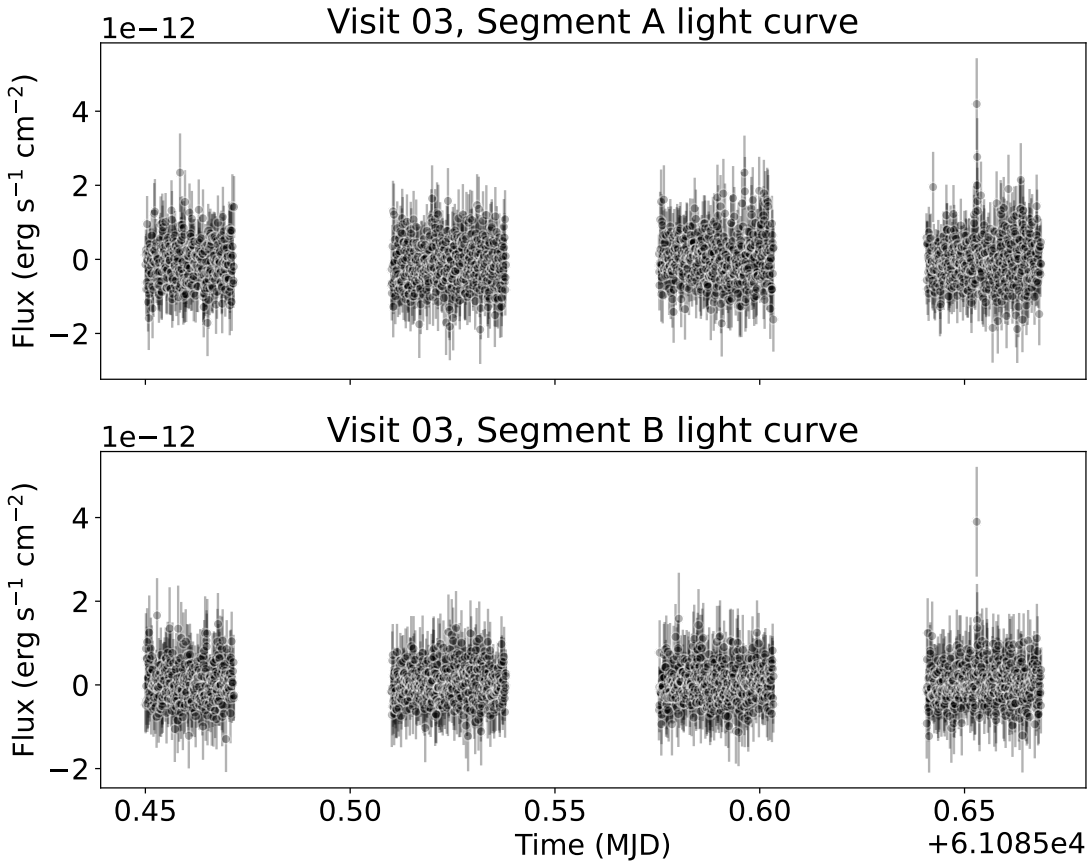

Figure 7: Light curves of Visit 3. Segment A corresponds to wavelengths [1230, 1365] Å and Segment B to [1140, 1214] Å.

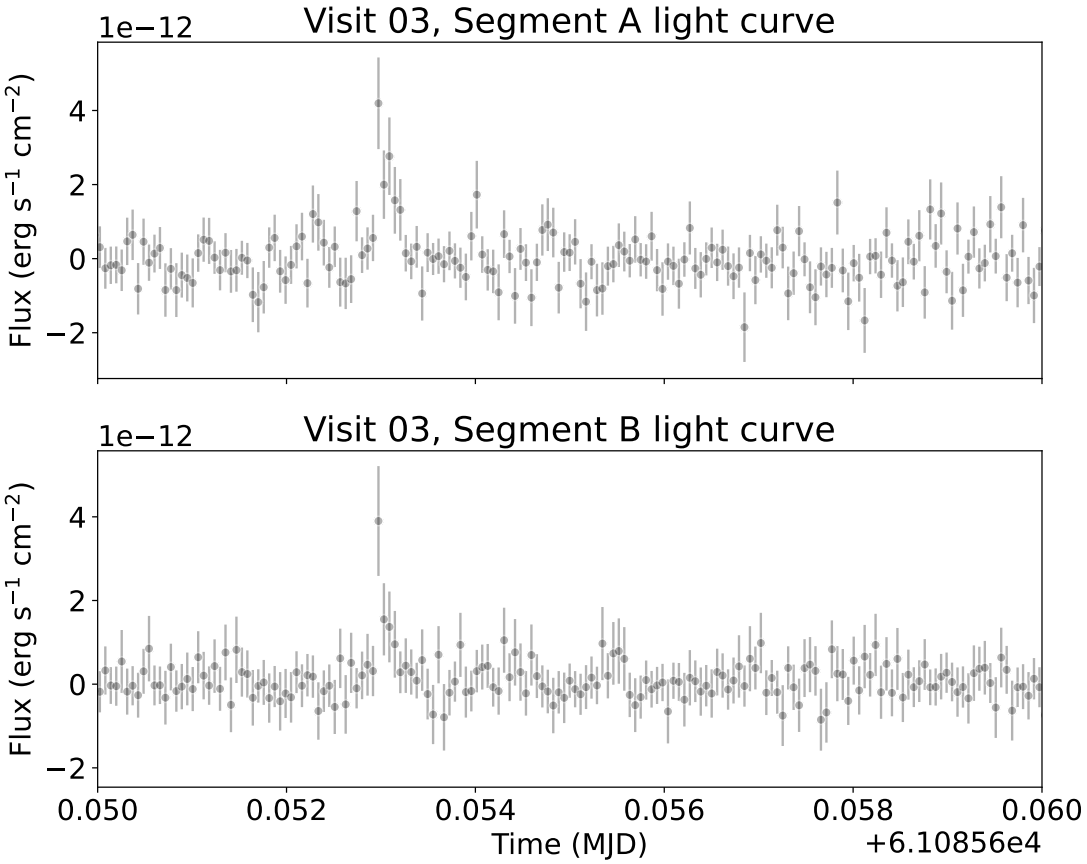

Figure 8: Zoom-in the light curves of Visit 3 near the detected potential flare.

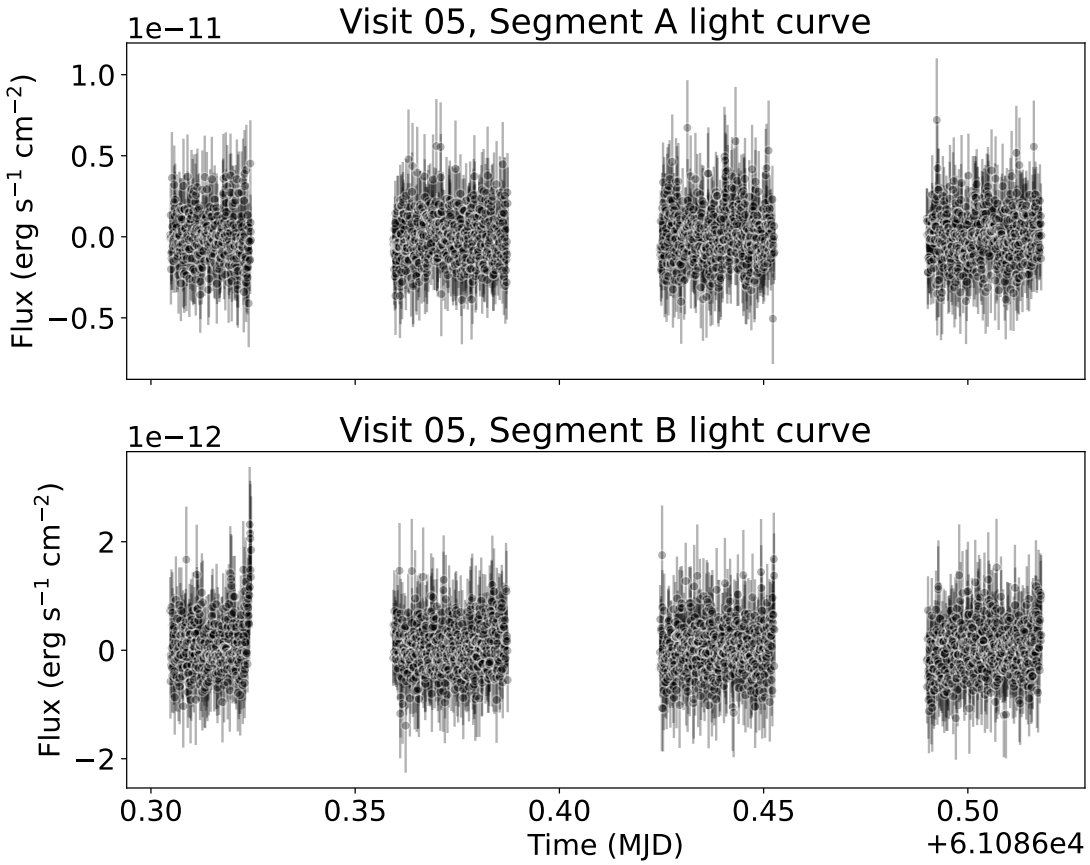

Figure 9: Light curves of Visit 5. Segment A corresponds to wavelengths [1550, 1700] Å and Segment B to [1350, 1520] Å.

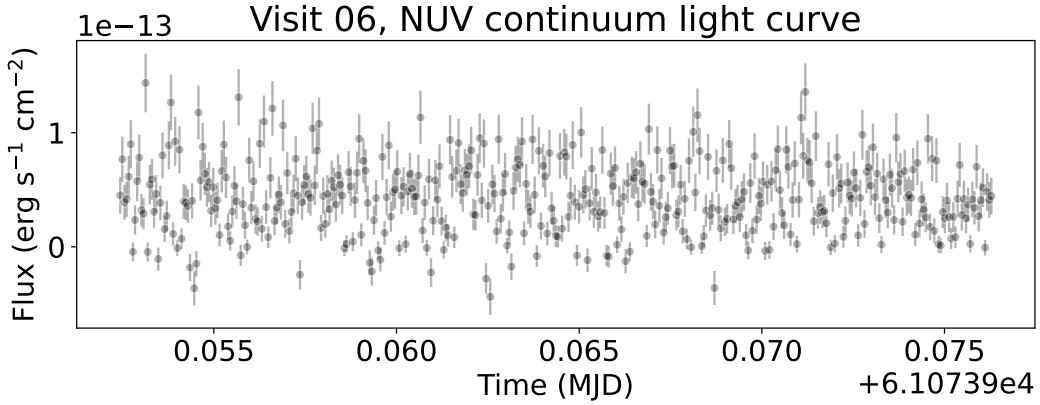

Figure 10: Light curve of Visit 6. The flux is integrated between wavelengths [1700, 3100] Å.

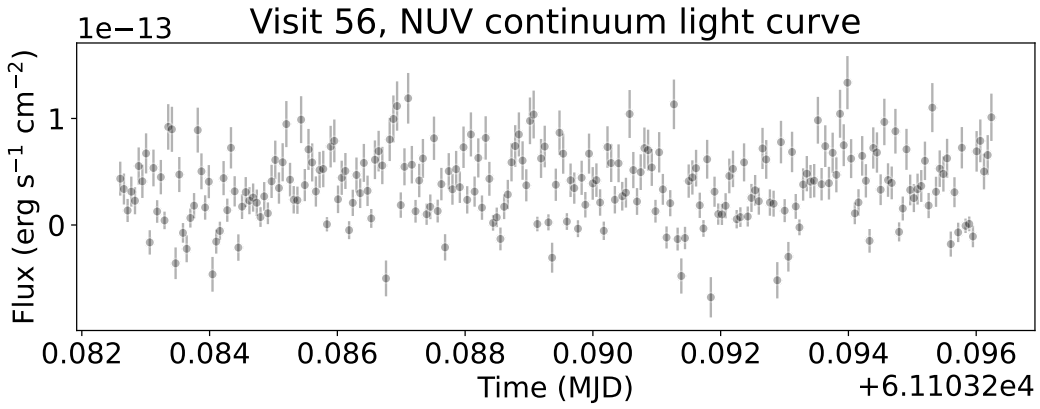

Figure 11: Light curve of Visit 56. The flux is integrated between wavelengths [1700, 3100] Å.

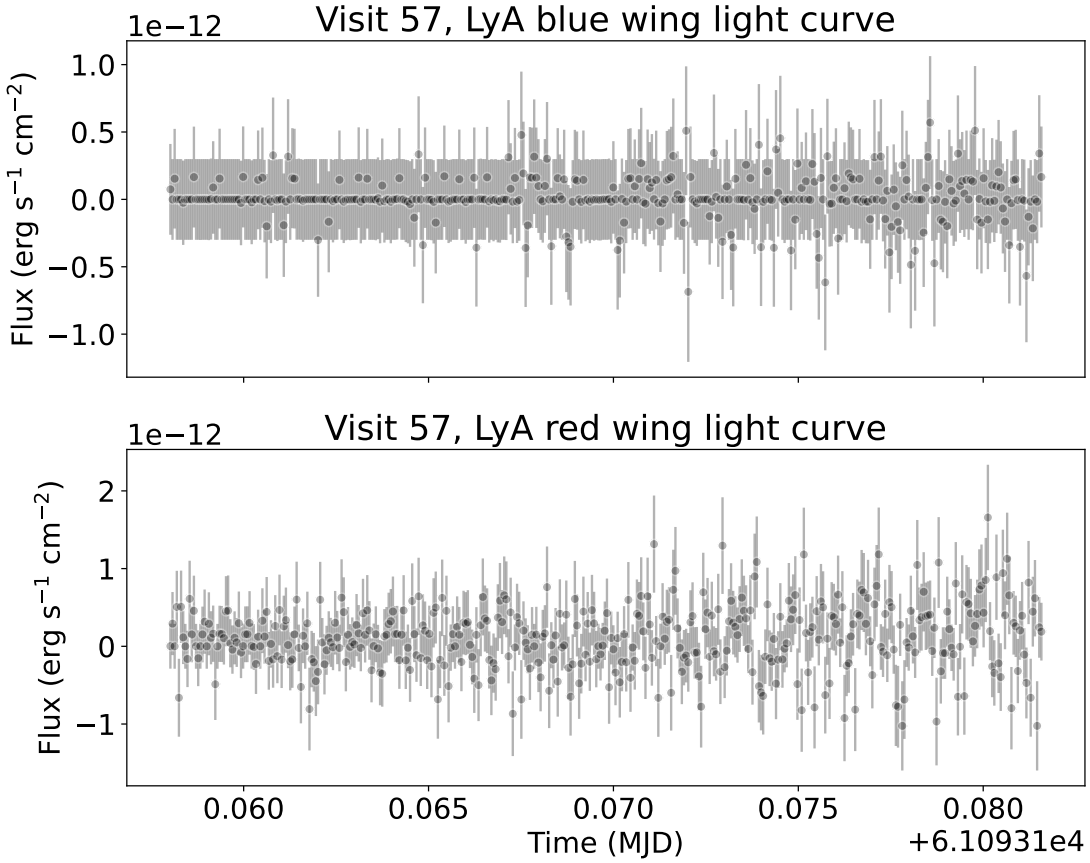

Figure 12: Light curves of Visit 57. The blue wing corresponds to wavelengths [1214.0, 1215.3] Å and the reg wing to [1215.8, 1217.5] Å.

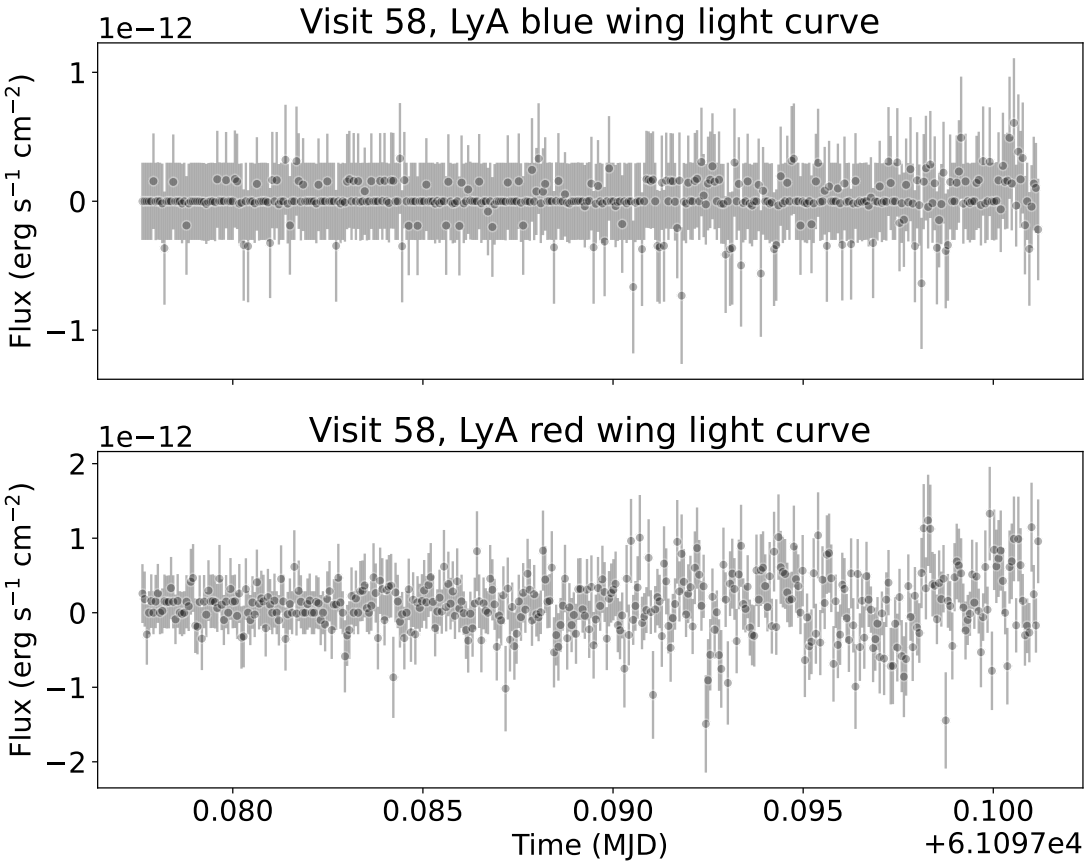

Figure 13: Light curves of Visit 58. The blue wing corresponds to wavelengths [1214.0, 1215.3] Å and the reg wing to [1215.8, 1217.5] Å.

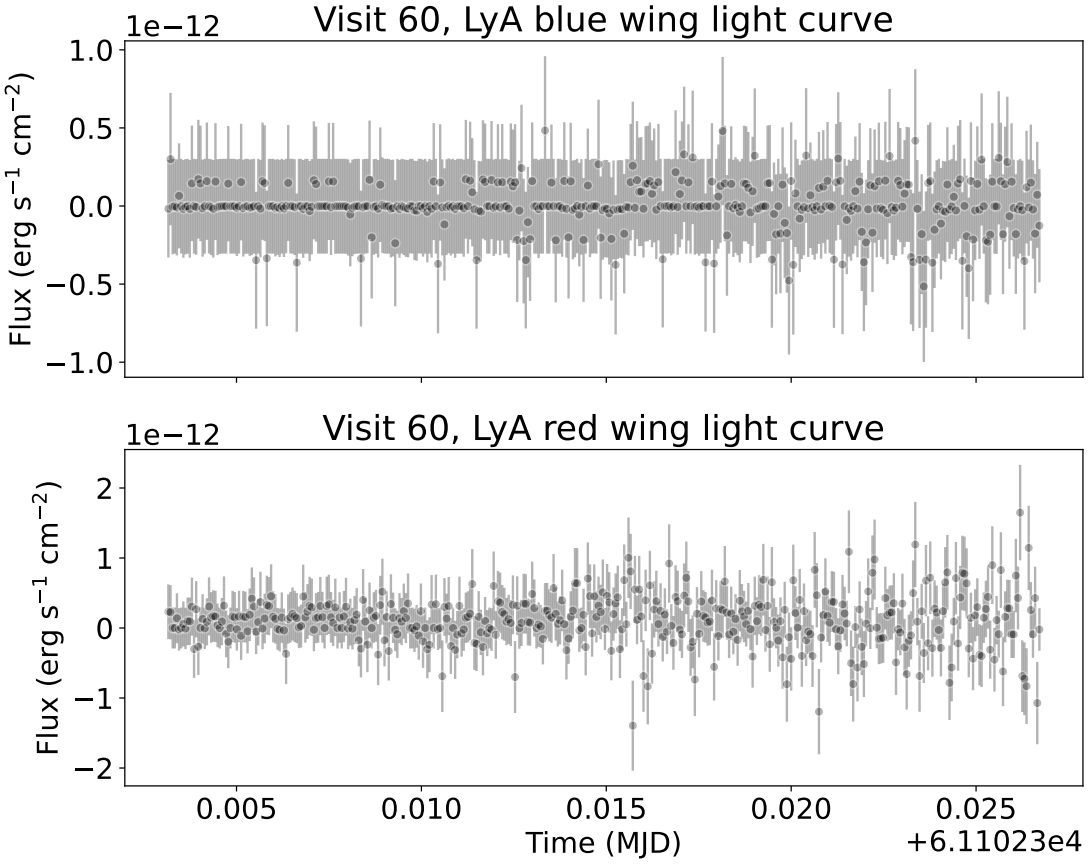

Figure 14: Light curves of Visit 60. The blue wing corresponds to wavelengths [1214.0, 1215.3] Å and the reg wing to [1215.8, 1217.5] Å.

Appendix

We present below the HST pointing jitter vectors of all the visits in this report. We do not observe any significant trends that could potentially affect the quality of the observations.

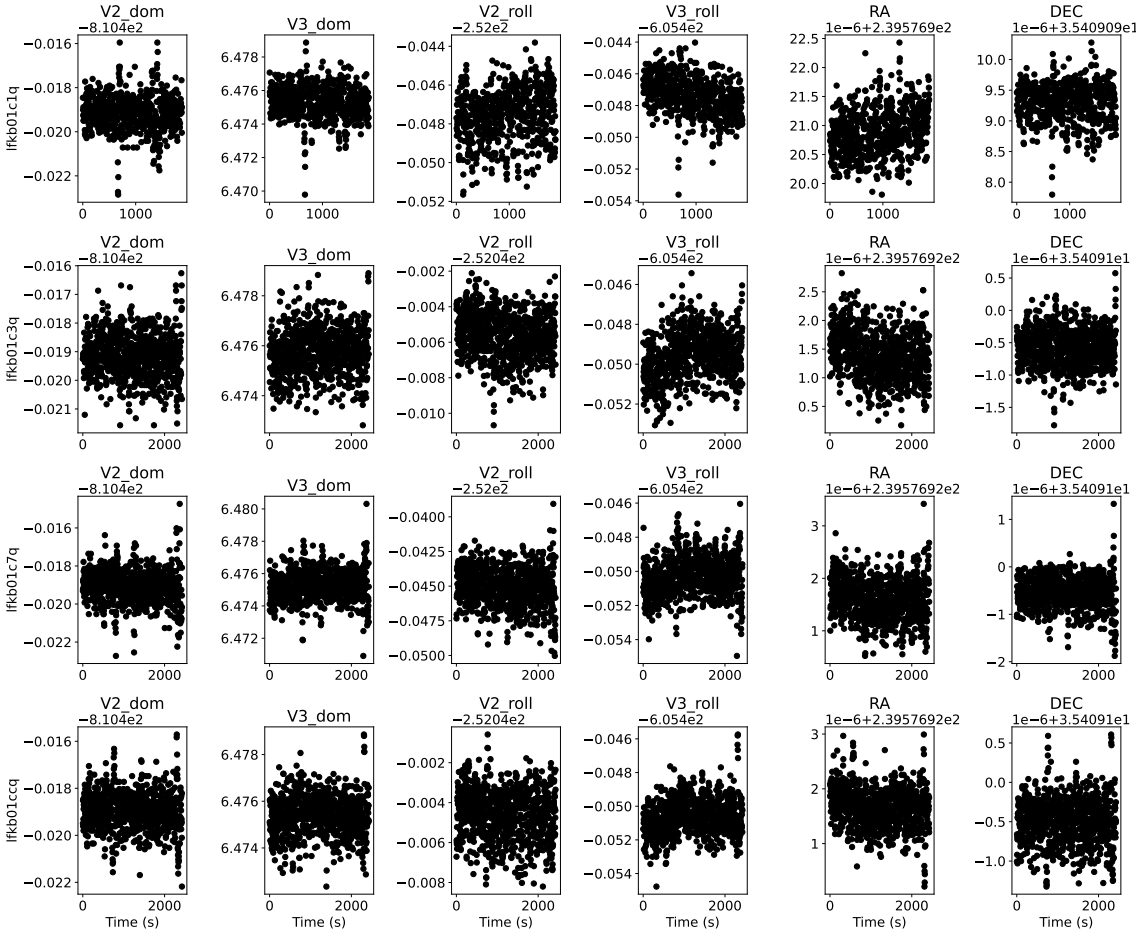

Figure 15: Jitter vectors for exposures in Visit 1.

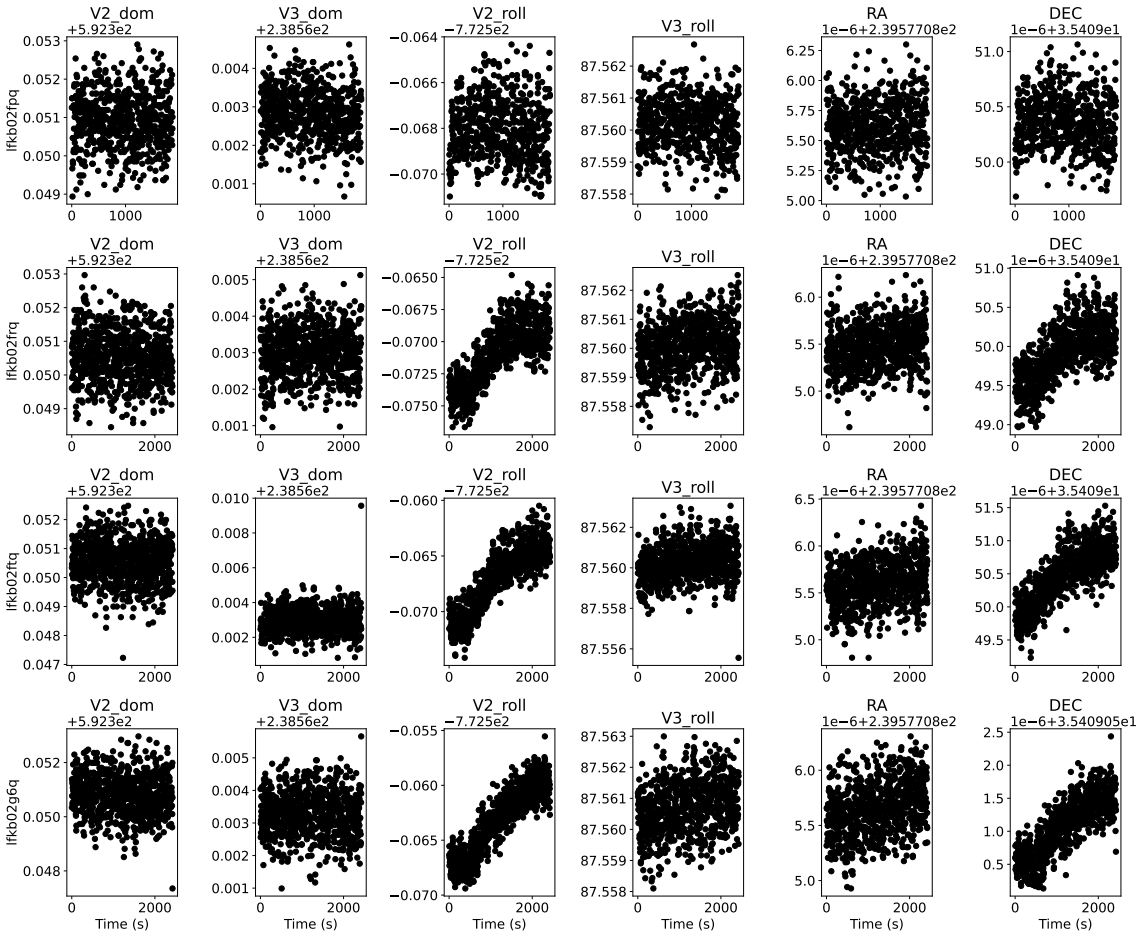

Figure 16: Jitter vectors for exposures in Visit 2.

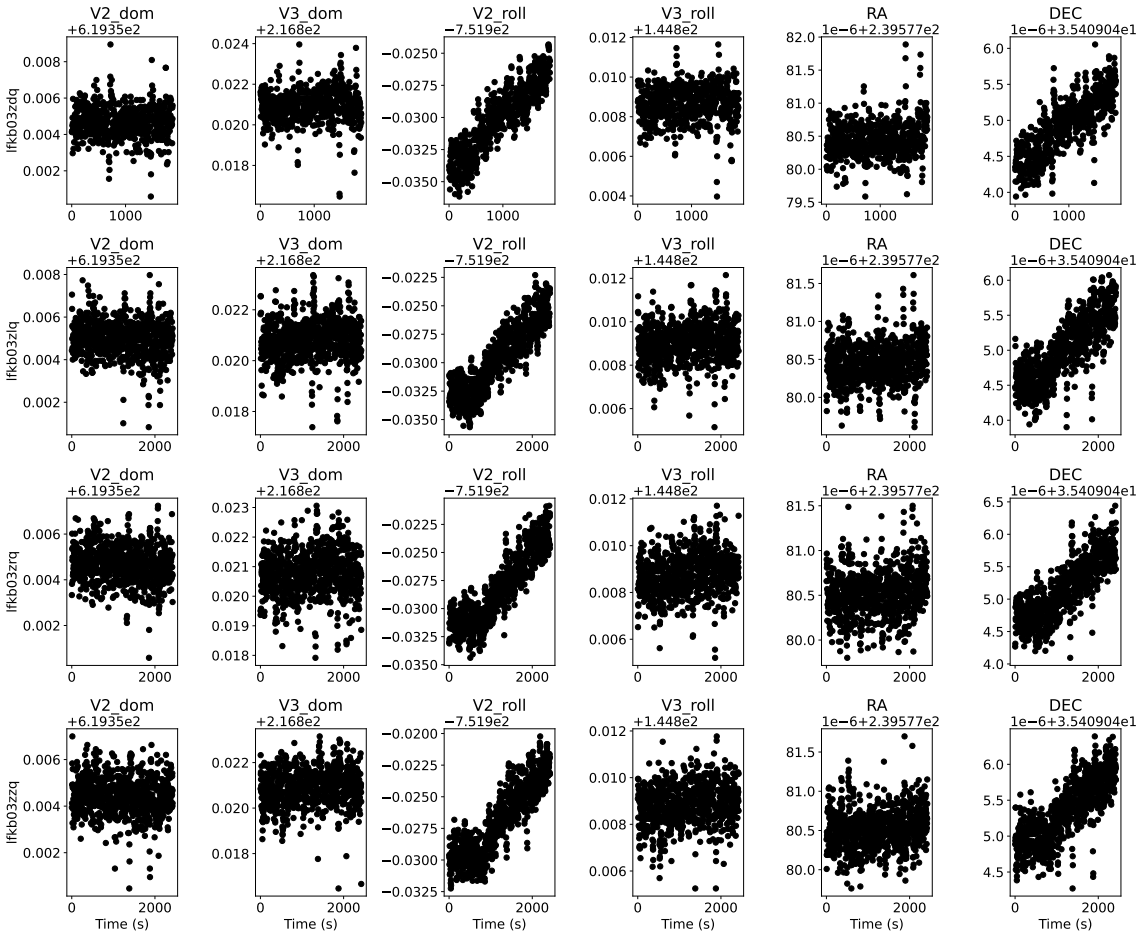

Figure 17: Jitter vectors for exposures in Visit 3.

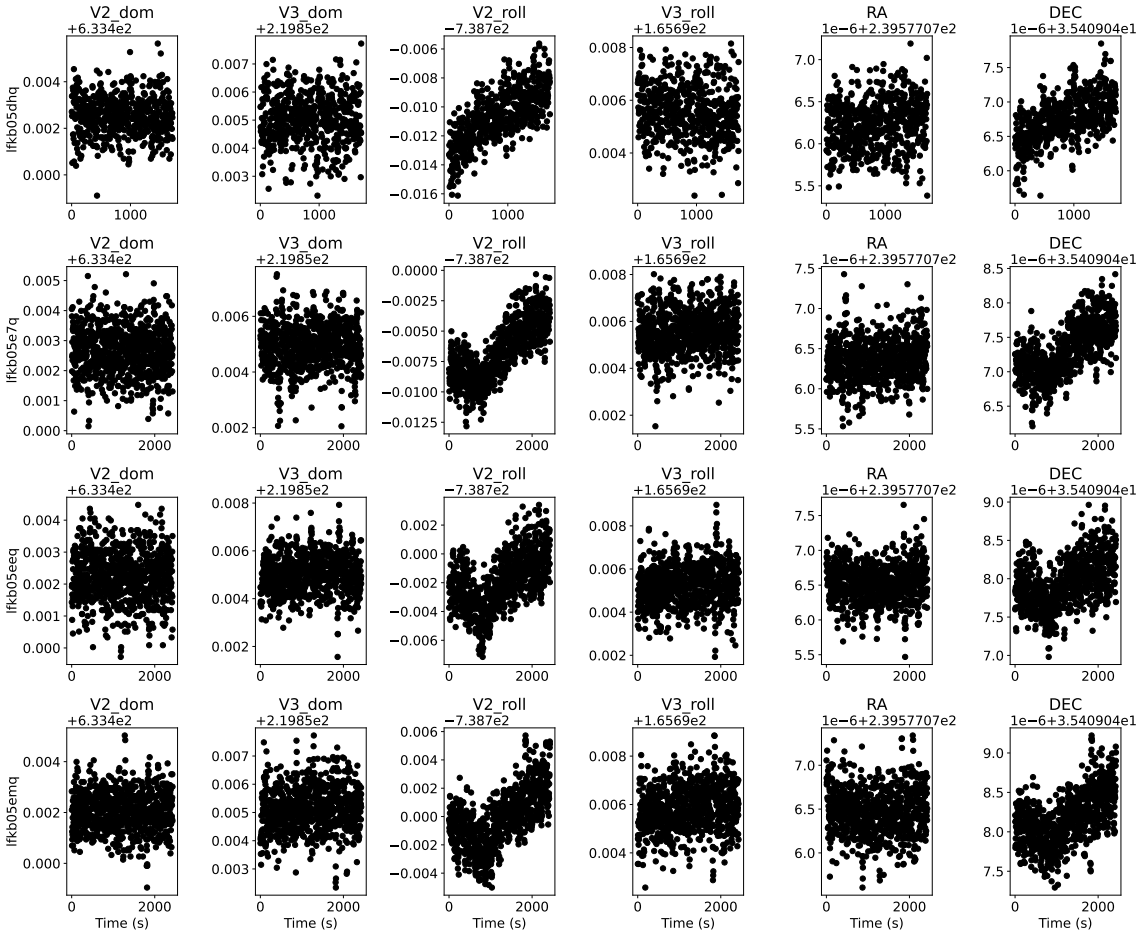

Figure 18: Jitter vectors for exposures in Visit 5.

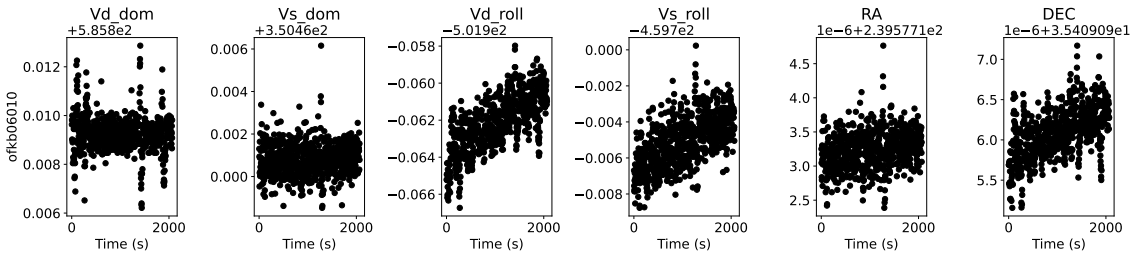

Figure 19: Jitter vectors for exposures in Visit 6.

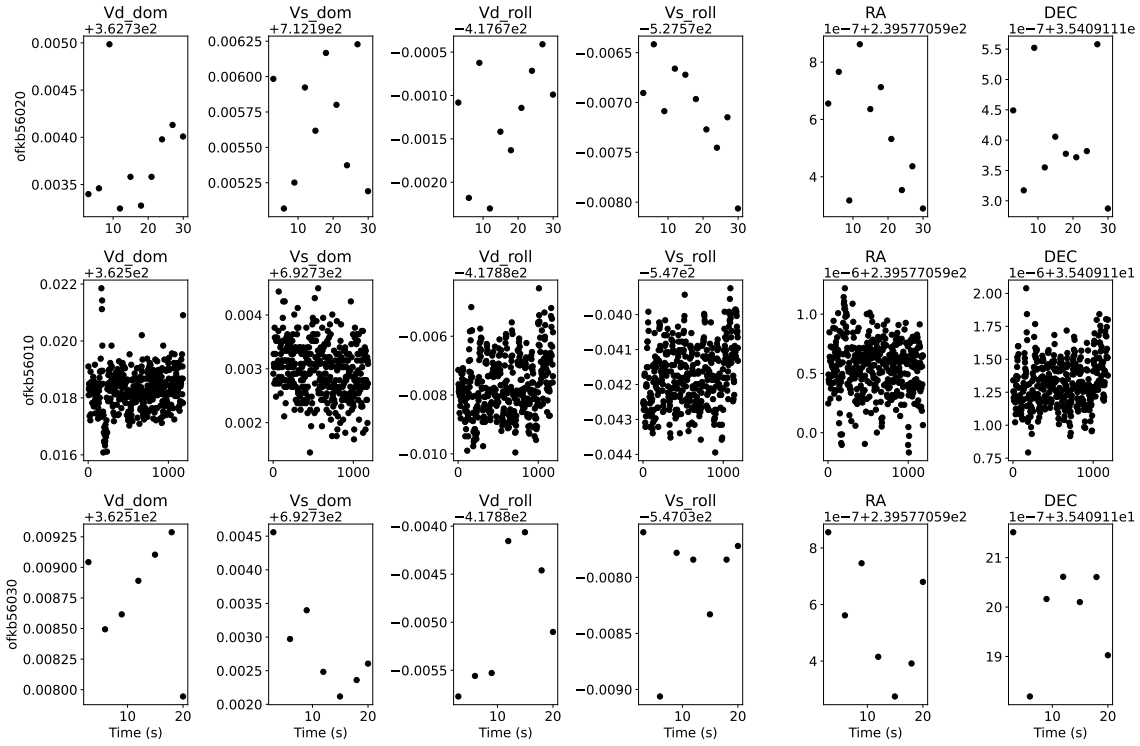

Figure 20: Jitter vectors for exposures in Visit 56.

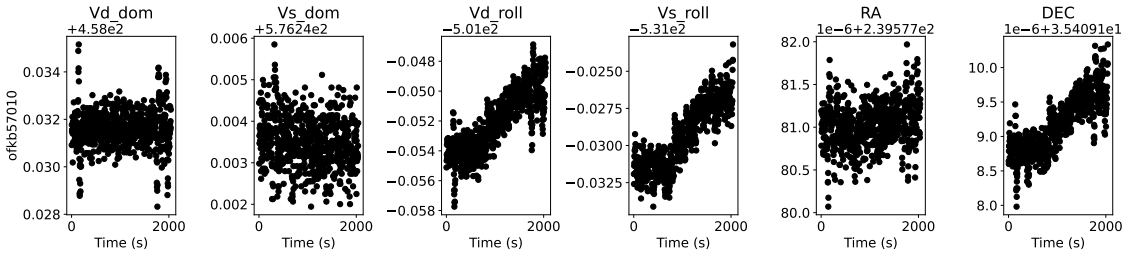

Figure 21: Jitter vectors for exposures in Visit 57.

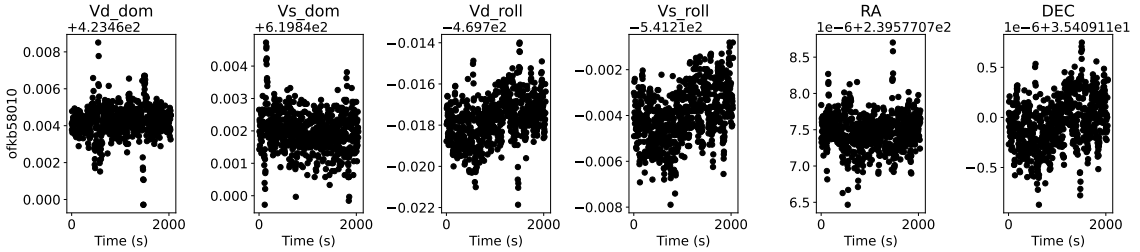

Figure 22: Jitter vectors for exposures in Visit 58.

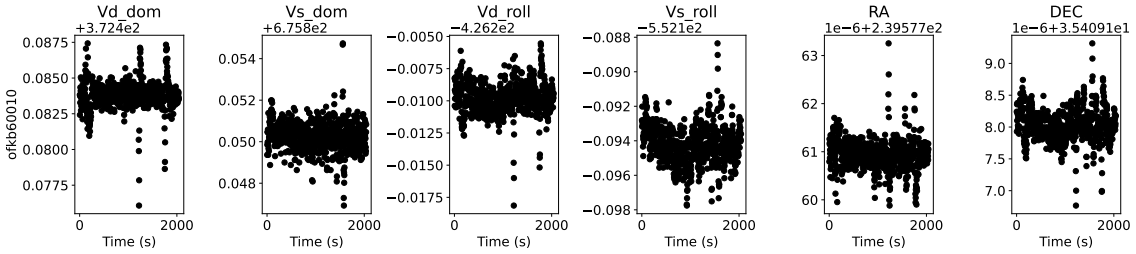

Figure 23: Jitter vectors for exposures in Visit 60.

References

Debes, J., Dos Santos, L., Espinoza, N., & Diamond-Lowe, H. 2025, Rocky Worlds DDT: HST Scheduling Report for GJ 3929, RWDDT Scheduling Reports

Dos Santos, L., Debes, J., Espinoza, N., & Diamond-Lowe, H. 2025, Rocky Worlds DDT: HST Data Analysis Report for GJ 3929, RWDDT Data Analysis Reports

Foreman-Mackey, D., Hogg, D. W., Lang, D., & Goodman, J. 2013, , 125, 306, doi: 10.1086/670067

Fouqué, P., Moutou, C., Malo, L., et al. 2018, , 475, 1960, doi: 10.1093/mnras/stx3246

Sankrit, R., Debes, J., Burger, M., et al. 2025, Overview of the new Hubble Spectroscopic Legacy Archive, Instrument Science Report COS 2025-18, 35 pages

Youngblood, A., France, K., Loyd, R. O. P., et al. 2016, ApJ, 824, 101, doi: 10.3847/0004-637X/824/2/101